## **Hailstone Shapes**

Laura Shedd, <sup>a</sup> Matthew R. Kumjian, <sup>a</sup> Ian Giammanco, <sup>b</sup> Tanya Brown-Giammanco, <sup>b</sup> and B. Ross Maiden <sup>b</sup>

<sup>a</sup> Department of Meteorology and Atmospheric Science, The Pennsylvania State University, University Park, Pennsylvania
<sup>b</sup> Insurance Institute for Business and Home Safety, Richburg, South Carolina

(Manuscript received 19 August 2020, in final form 23 October 2020)

ABSTRACT: Hailstone growth results in a variety of hailstone shapes. These shapes hold implications for modeling of hail processes, hailstone fall behaviors including fall speeds, and remote sensing signatures of hail. This study is an in-depth analysis of natural hailstone shapes, using a large dataset of hailstones collected in the field over a 6-yr period. These data come from manual measurements with digital calipers and three-dimensional infrared laser scans. Hailstones tend to have an ellipsoidal geometry with minor-to-major axis ratios ranging from 0.4 to 0.8, and intermediate-to-major axis ratios between 0.8 and 1.0. These suggest hailstones are better represented as triaxial ellipsoids as opposed to spheres or spheroids, which is commonly assumed. The laser scans allow for precise sphericity measurements, for the first time. Hailstones become increasingly nonspherical with increasing maximum dimension, with a typical range of sphericity values of 0.57 to 0.99. These sphericity values were used to estimate the drag coefficient, which was found to have a typical range of 0.5 to over 0.9. Hailstone maximum dimension tends to be 20%–50% larger than the equivalent-volume spherical diameter. As a step toward understanding and quantifying hailstone shapes, this study may aid in better parameterizations of hail in models and remote sensing hail detection and sizing algorithms.

KEYWORD: Hail

### 1. Introduction

Natural hailstones take on a rich variety of shapes depending on their growth history, trajectory, and fall behavior through their parent storm. In particular, strikingly prominent lobes or protuberances are possible when hailstones undergo vigorous wet growth (e.g., Knight and Knight 1970). Dry growth conditions may render smaller-scale perturbations or cusped lobes (Browning 1966; Knight and Knight 1970) across the hailstone's surface, as well. Despite this natural variability, hailstones are represented as or assumed to be spheres or spheroids in a wide range of applications, including hailstone growth and melting models (e.g., Ziegler et al. 1983; Nelson 1983; Rasmussen and Heymsfield 1987; Adams-Selin and Ziegler 2016; Dennis and Kumjian 2017; Kumjian and Lombardo 2020), radar-based hail detection and sizing algorithms (e.g., Ryzhkov et al. 2013a,b; Ortega et al. 2016), and microphysics parameterization schemes employed in numerical weather prediction models (e.g., Hong and Lim 2006; Thompson et al. 2004; Morrison and Milbrandt 2015).

Hailstone shape matters for a number of reasons. For example, it affects the thermal energy transfer to and from the environment (e.g., Macklin 1963; Browning 1966; Bailey and Macklin 1968a; Schuepp and List 1969), which governs hailstone growth and melting rates in models (e.g., Nelson 1983; Rasmussen and Heymsfield 1987; Kumjian and Lombardo 2020). A hailstone's shape—including irregularities and protuberances—also affect its electromagnetic scattering properties (Jiang et al. 2019), which has important implications for

Corresponding author: Matthew R. Kumjian, kumjian@psu.edu

radar- or satellite-based hail detection algorithms. An irregular particle's shape affects its drag coefficient (e.g., Chhabra et al. 1999), and thus fall speed and fall behavior (i.e., tumbling, gyrating, etc.). Hailstone fall speed is an important determinant of its kinetic energy and thus damage potential (Heymsfield et al. 2018), and its falling behavior in turn affects its scattering properties for polarimetric radar (e.g., Ryzhkov et al. 2011; Kumjian 2018). Further, parameterizations of hail fall speed play an important role in simulations of convective storm structure and life cycle (e.g., Morrison and Milbrandt 2011; Bryan and Morrison 2012).

However, despite its importance, only a few studies have quantified the shape of natural hailstones (e.g., Barge and Isaac 1973; Macklin 1977; Knight 1986). This is in large part owing to the difficulty in measuring the often highly irregular shapes of natural hailstones, necessitating simplified models. For example, Barge and Isaac (1973) and Knight (1986) investigated hailstone minor-to-major axis ratios, but characterizing hailstones with a single aspect ratio implicitly assumes a spheroidal shape. More recent field campaigns, such as the Insurance Institute for Business and Home Safety (IBHS) Hail Project (Brown-Giammanco and Giammanco 2018), have begun measuring three orthogonal axes for hailstones, thereby implicitly assuming an ellipsoidal shape.

In this paper, we present an analysis of a more comprehensive dataset of these natural hailstone shapes. The recent advent of infrared laser scanning technology also makes it possible to obtain high-resolution three-dimensional (3D) renderings of hailstone shapes (Giammanco et al. 2017), including precise measurements of natural hailstone volume and surface area, for the first time. Here, we report on two characteristic axis ratios for a large population of hailstones,

quantify the relationship between hailstone maximum dimension and equivalent-volume spherical diameter, hailstone sphericity, and discuss implications of how hailstone roughness and irregularities potentially affect thermal energy transfer and drag coefficients.

### 2. Data and methods

Since 2012, IBHS has conducted an annual field project sampling hailstones in the U.S. Great Plains, and partnered with The Pennsylvania State University (PSU) beginning in 2015. The experiment has sampled more than 3600 hailstones on 42 different days (Table 1) from a large region of the central United States (Fig. 1). Additional samples come from a hail event at the IBHS research center in South Carolina. The hailstones were collected from the ground after the passage of their parent storm, and the major  $(D_{\text{max}})$  and minor  $(D_{\text{min}})$ axes were measured manually using digital calipers. Starting in 2014, a third dimension ("intermediate" dimension,  $D_{int}$ ) was measured, as well. This intermediate dimension was taken orthogonal to the plane containing the major and minor axes, to the best of the project participants' abilities. The distribution of hailstone  $D_{\text{max}}$  measurements is shown in Fig. 2a; they range from < 0.5 cm to nearly 12 cm, with the vast majority <5 cm.

As part of the data collection efforts, IBHS has introduced 3D infrared laser scanning capabilities to provide highresolution digital models of hailstone shapes (Giammanco et al. 2017). These digital models are used herein to provide more detailed information about hailstone shapes. Such 3D scanning has been used to document and preserve information on giant hailstones (Kumjian et al. 2020) and to compute electromagnetic scattering calculations for natural hailstone shapes (Jiang et al. 2019). Since 2015, 150 hailstones have been scanned, including plaster casts of several record hailstones: Coffeyville, Kansas; Aurora, Nebraska; and Vivian, South Dakota. The 3D-scanned stones ranged in maximum dimension from 1.79 to 16.90 cm (Fig. 2b). In general, these are larger than the manually measured hailstones given the limitations of the 3D-scanner system (the mount used to support the hailstones could not hold stones <1 cm in maximum dimension; see Giammanco et al. 2017) and the time needed to scan a stone, given that smaller hailstones would melt. An example of some of these 3Dscanned hailstones is shown in Fig. 3, with their  $D_{\text{max}}$  shown in Table 2.

Many (n=118) of the 3D-scanned hailstones were also manually measured with digital calipers, affording us the opportunity to estimate the caliper measurement error, considering the 3D-scanned measurement as "truth" for the three hailstone dimensions. The distribution of these errors, defined as the 3D-scanned dimension minus the caliper measurement, are centered on approximately 0 mm for  $D_{\rm max}$ ,  $D_{\rm int}$ , and  $D_{\rm min}$  (Fig. 4), with median errors of 0.46, -0.08, and 0.87 mm, respectively. The RMSE values for these three dimensions are 2.83, 6.69, and 5.70 mm, respectively. These values suggest the digital caliper measurements are unbiased, and that the  $D_{\rm max}$  measurements are most accurate;  $D_{\rm min}$ 

TABLE 1. Numbers of hailstones collected over the 6-yr time span as part of the IBHS field project. There is a discrepancy between the total number of hailstones in the dataset and the total number represented per year. This is because there are 33 stones in the dataset without a specified date or time. Adding those in brings the total number to the 3689 value that is seen elsewhere throughout the study.

Year	Hailstones	Collection days	April days	May days	June days
2012	238	7	0	3	4
2013	683	7	0	5	2
2014	1626	7	0	3	4
2015	272	3	0	3	0
2016	323	8	0	5	3
2017	514	10	1	4	5
Total	3656	42	1	23	18

measurements are the least accurate. These 118 hailstones were included in both datasets, though with independent measurements: calipers versus 3D scans. As such, we should expect relatively good agreement between the statistics from both datasets, aforementioned measurement errors notwithstanding. Though we show both datasets separately in the analysis below, our conclusions are based on the combined data.

For the manually measured hailstones, both the minimum aspect ratio  $\varphi_{\min} = D_{\min}/D_{\max}$  and intermediate aspect ratio  $\varphi_{\text{int}} = D_{\text{int}}/D_{\max}$  were calculated. From 2012 through part of 2014, only two dimensions were measured in the field, and so for those hailstones (n = 1730), only a minimum aspect ratio could be calculated. For the remainder of the dataset (n = 1959), and for the 3D-scanned stones (n = 150), both aspect ratios were calculated.

We can obtain several additional quantities of interest, including the hailstone equivalent-volume spherical diameter,  $D_{\rm eq}$ , defined as the diameter of a sphere with the same volume as the hailstone, the surface area of this equivalent-volume sphere,  $SA_{\rm eq}$ , and the actual hailstone surface area,  $SA_{\rm msr}$ . For the manually measured hailstones, we obtained  $D_{\rm eq}$  from their estimated volume, V. For hailstones with three measured axes, ellipsoidal geometry was used:

$$V = \frac{\pi}{6} (D_{\text{max}} \times D_{\text{min}} \times D_{\text{int}}), \tag{1}$$

whereas for the hailstones with two measured axes, oblate spheroidal geometry was used (e.g., Knight 1986):

$$V = \frac{\pi}{6} (D_{\text{max}} \times D_{\text{max}} \times D_{\text{min}}). \tag{2}$$

These volumes were then used to obtain  $D_{eq}$  and  $SA_{eq}$ .

To determine  $SA_{msr}$ , we used an expression for the oblate spheroidal surface area  $SA_{obl}$  (Beyer 2002) in the case of two-axis measurements:

$$SA_{obl} = \frac{\pi D_{max}^2}{2} + \frac{\pi D_{min}^2}{4\varepsilon} \ln\left(\frac{1+\varepsilon}{1-\varepsilon}\right), \tag{3}$$

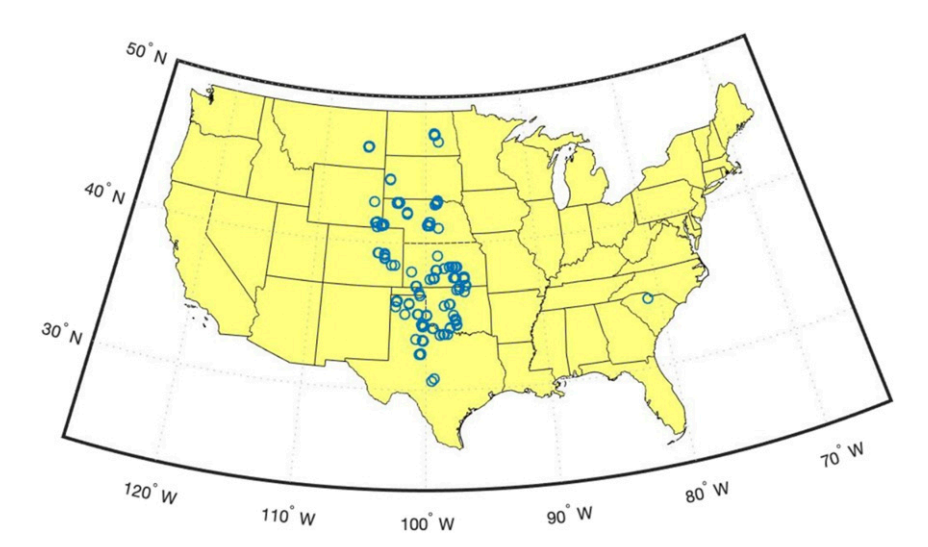


FIG. 1. Map of the continental United States with the collection locations of hailstones over the 6-yr span plotted as blue circle markers. Most of the locations have multiple hailstones at each location.

where  $\varepsilon = \sqrt{1-\varphi_{min}^2}$  is the eccentricity, or, in the case of three-axis measurements, we used the Thomsen–Cantrell formula for the ellipsoidal surface area  $SA_{ell}$ :

$$SA_{ell} \approx \pi \left[ \frac{(D_{max}D_{int})^{1.6} + (D_{max}D_{min})^{1.6} + (D_{int}D_{min})^{1.6}}{3} \right]^{1/1.6}.$$
(4)

For the 3D-scanned hailstones, precise V and  $SA_{msr}$  values were obtained directly from the scanner measurements. The  $D_{\rm eq}$  and  $SA_{\rm eq}$  directly follow from the measured V.

We also calculated sphericity  $\Psi$  (Wadell 1935):

$$\Psi = \frac{SA_{eq}}{SA_{msr}}$$
 (5)

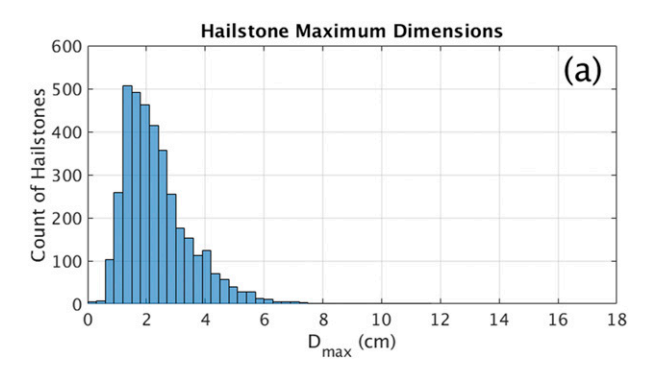
for both datasets. In essence,  $\Psi$  is a measure of the hailstone's shape irregularity. For example, a smooth, spherical hailstone has  $\Psi=1$ , whereas a smooth oblate spheroidal hailstone with  $\varphi_{\min}=0.7$  (e.g., Knight 1986) has  $\Psi=0.977$ . Note that  $\Psi^{-1}$  can be considered the "surface area enhancement" over the equivalent-volume sphere, so the spheroidal hailstone just described would have a surface area 2.4% greater than a sphere of the same volume. Further, a smooth ellipsoidal hailstone with  $\varphi_{\min}=0.7$  and  $\varphi_{\inf}=0.85$  has  $\Psi\sim0.983$ . Thus,  $\Psi$  values substantially less than  $\sim\!0.98$  suggest irregular shapes and/or surfaces compared to smooth spheroidal or ellipsoidal hail of typical axis ratios. The  $\Psi$  values for the sample hailstones in Fig. 3 are also provided in Table 2 for reference.

Given the assumed spheroidal or ellipsoidal shape used to characterize the manually measured hailstones, we expect the reported  $\Psi$  values to be underestimates, as they do not account for the sometimes highly irregular lobe structures on real hailstones. The 3D-scanned hailstones provide more robust  $\Psi$  estimates given the precision of their surface area measurements.

### 3. Analysis and results

### a. Aspect ratios

Figure 5 shows 2D kernel density estimates (KDE) of the distributions of aspect ratios as a function of  $D_{\rm max}$  for both sets of hailstones. The highest density of data for the manually measured hailstones  $\varphi_{\rm min}$  (Fig. 5a) lies between 0.4 and 0.8,



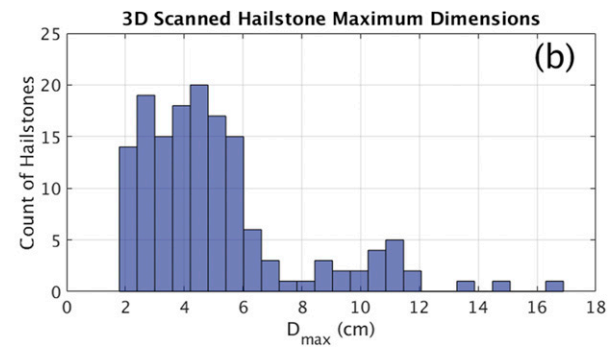


FIG. 2. Plot of the natural hailstone maximum dimension ( $D_{\text{max}}$ ) distributions for (a) manually measured hailstones, where n = 3689, and (b) 3D-scanned hailstones, where n = 150.

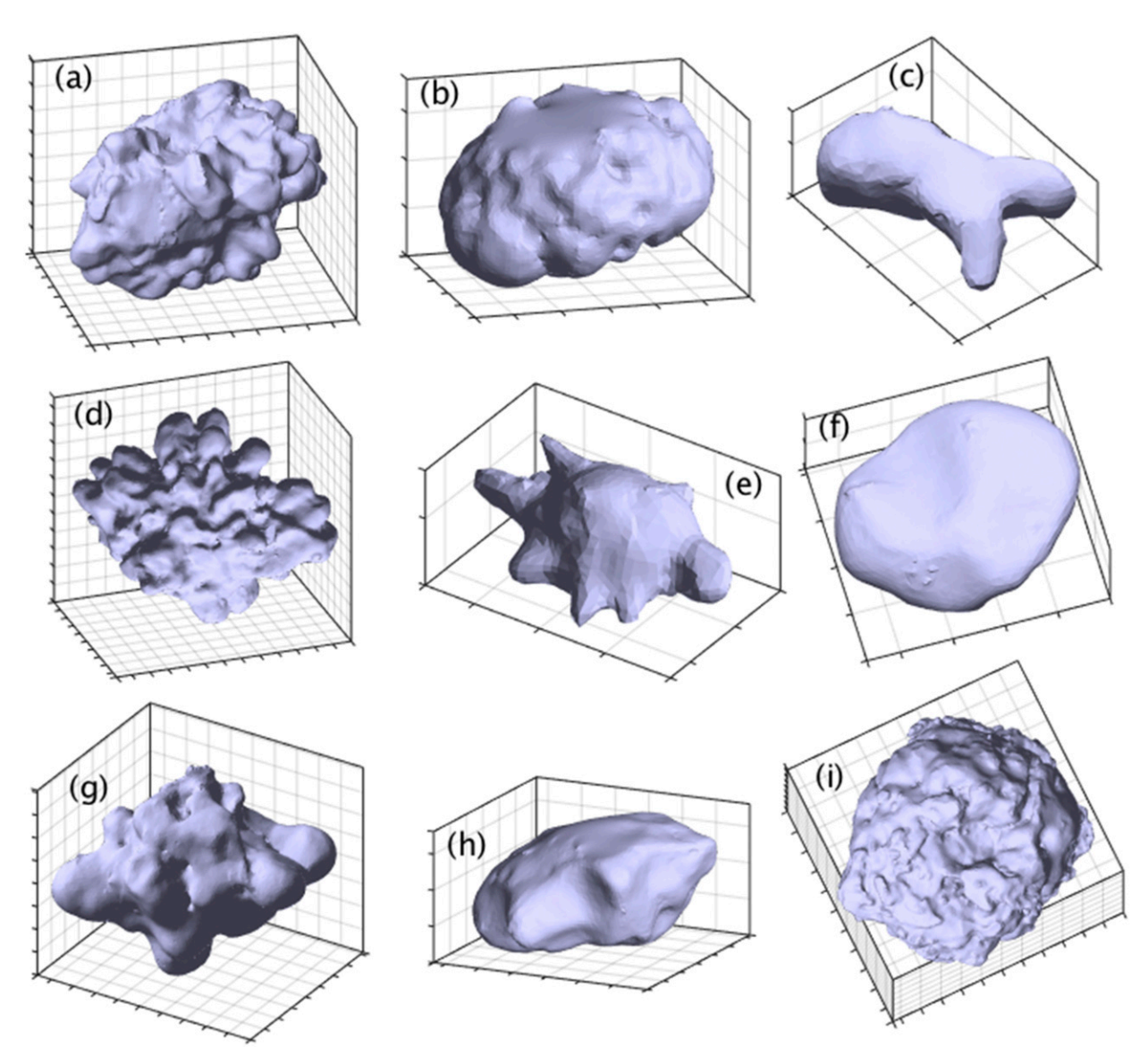


FIG. 3. Examples of 3D-scanned hailstones. In each, the grid boxes represent 1 cm. These were selected from the dataset to highlight hailstone shape diversity and to show some particularly noteworthy examples.

peaking between 0.6 and 0.65. Similarly, the 3D-scanned stones have  $\varphi_{\min}$  values peaking between 0.5 and 0.6 (Fig. 5c). These maxima are collocated with some of the smaller hailstone sizes (<4 cm) for the manually measured hailstones and between 2 and 6 cm for the 3D-scanned hailstones, given the distribution of  $D_{\max}$  for these two datasets. For both datasets, some hailstones have a  $\varphi_{\min}$  as low as 0.2 or as high as 1. In the case of the  $\varphi_{\rm int}$  (Figs. 5b,d), the highest density of data is between 0.8 and 1. Some  $\varphi_{\rm int}$  values were as low as 0.4 for both datasets and as low as <0.2 in some isolated instances for the manually measured hailstones. Taken together, there is some evidence of decreasing aspect ratio values with increasing  $D_{\rm max}$ . The modest positive correlations observed between the  $D_{\rm int}$  errors and  $D_{\rm int}$  (r=0.69; Fig. 4b), and between the  $D_{\rm min}$  errors and  $D_{\rm min}$  (r=0.53; Fig. 4c) suggest measurement errors would

contribute to overestimates of  $\varphi_{\rm int}$  and  $\varphi_{\rm min}$  for smaller hailstones, and underestimates for larger hailstones. Such errors could contribute to the observed relationship of decreasing aspect ratios with increasing  $D_{\rm max}$ ; however, these errors are less correlated with  $D_{\rm max}$  (r=0.40 and 0.22, respectively). Thus, the digital caliper error characteristics are unlikely to be a dominant contributor to the observed relationship.

We can further elucidate this relationship by determining the variability of the hailstone  $\varphi_{\min}$  with increasing  $D_{\max}$ . Knight (1986) analyzed  $\varphi_{\min}$  as a function of  $D_{\max}$  using photographs of hailstone slices from Colorado, Oklahoma, and Alberta, Canada. Figure 6 shows the results from the Knight (1986) study along with the manually measured hailstones used for this study. Similar to the Knight (1986) study, the manually measured hailstones were binned into size ranges of 5 mm,

TABLE 2. Hailstone shape properties for the sample of 3D-scanned stones shown in Fig. 3. These include equivalent-volume spherical diameter ( $D_{\rm eq}$ , in mm), maximum dimension ( $D_{\rm max}$ , in mm), and sphericity ( $\Psi$ ).

Panel in Fig. 3	$D_{ m eq}$	$D_{ m max}$	$\Psi$
a	76.5	117.4	0.682
b	44.9	58.6	0.837
c	19.9	39.0	0.742
d	85.2	136.2	0.612
e	19.9	37.7	0.791
f	31.1	47.2	0.809
g	64.8	110.2	0.690
h	48.4	68.8	0.866
i	89.8	113.7	0.719

with any hailstone >61 mm in the same bin owing to the small sample size above that  $D_{\max}$ . The mean  $\varphi_{\min}$  value for the given range of sizes is plotted along with a bias-corrected and accelerated bootstrapped 95% confidence interval about this mean value using 2000 iterations (Efron and Tibshirani 1993). The Knight (1986) 95% confidence intervals about the mean are also shown. In every panel of Fig. 6, the manually measured hailstones  $\varphi_{\min}$  were below that of Knight (1986), though the variability in each bin is consistent with that found in Knight (1986). Though the errors in  $D_{\min}$  measurements made with digital calipers were the largest (see section 2), and thus would propagate uncertainty into the  $\varphi_{\min}$  estimates, we can rule out a systematic bias in the measurements large enough to explain the discrepancy: recall the median error magnitude was <1 mm. We speculate on a possible reason for this discrepancy in the next section. Both datasets, however, do indicate a decreasing trend of the aspect ratio with increasing  $D_{\text{max}}$ . Knight (1986) found mean  $\varphi_{\text{min}}$  values ranging from 0.86 to 0.95 for hailstones with  $1 < D_{\text{max}} < 5 \text{ mm}$ , which decreased to a range of 0.58–0.75 for hailstones with  $56 < D_{\text{max}} < 60 \text{ mm}$ ; these values represent the range of means for all three of their sample locations. In contrast, our data show  $\varphi_{min}$  of 0.76 for the  $1 < D_{\rm max} < 5$  mm size interval, decreasing to 0.49 for  $D_{\rm max} >$ 61 mm. In all cases,  $\varphi_{\min}$  declines by >0.15 for the full range of  $D_{\text{max}}$  values; averaging Knight's three datasets with ours results in a decline of 0.25 across the range of  $D_{\text{max}}$  values.

The joint distribution of aspect ratios ( $\varphi_{\min}$ ,  $\varphi_{\inf}$ ) are shown in Fig. 7, along with comparisons to oblate and prolate spheroids. For the manually measured hailstones (Fig. 7a), only the stones with three nonidentical measurements were used, resulting in n=1528. The highest density of data is located between these two annotated lines, suggesting hailstones typically are triaxial ellipsoids (or scalene oblate spheroids), with  $\varphi_{\inf}$  between 0.8 and 0.9 (modal value of 0.84), and  $\varphi_{\min}$  between 0.5 and 0.7 (modal value of 0.63). These measurements agree well with Macklin (1977), who reported the findings of various studies that collectively suggest hailstones tend to be

triaxial ellipsoids with only 10%–20% difference in the length of the two major axes (i.e., a  $\varphi_{\rm int}$  of 0.8 to 0.9), and  $\varphi_{\rm min}$  down to 0.5.

### b. $D_{\text{max}}$ versus $D_{\text{eq}}$

Figure 8 shows  $D_{\rm max}$  versus  $D_{\rm eq}$  for the manually measured hailstones. A strong positive correlation is evident. Again using a bias-corrected and accelerated bootstrapping technique (Efron and Tibshirani 1993) with 2000 iterations to compute the 95% confidence interval about the linear correlation coefficient, we find r=[0.895,0.940]. A linear fit to the data is also provided in the figure, and has an RMSE of 4.2 mm. The slope of this fitted line (1.175) indicates that  $D_{\rm max}$  tends to be ~20% larger than  $D_{\rm eq}$ . The bootstrapped (n=2000 iterations) 95% confidence interval about this slope of the best-fit line is [1.1596, 1.1960].

Given the imposed assumption of ellipsoidal geometry for the manually measured hailstone dataset, the volume of these stones, and thus  $D_{\rm eq}$ , may be overestimated. An overestimation of  $D_{\rm eq}$  would lead to an underestimation of the slope of the best-fit line. Giammanco et al. (2015) faced the same issue when estimating hailstone densities: overestimated volume and  $D_{\rm eq}$  combined with their mass measurements led to inaccurate estimates of hailstone density.

The relationship between  $D_{\rm eq}$  and  $D_{\rm max}$  for the 3D-scanned stones is shown in Fig. 9. Again, a linear relationship reveals a very good fit as suggested by a high correlation coefficient r=[0.950,0.978], though with larger RMSE (7.2 mm), compared to the larger dataset of manually measured hailstones. Interestingly, the slope of the fitted line is greater for the 3D-scanned stones, indicating that  $D_{\rm max}$  is ~40% larger than  $D_{\rm eq}$  for these stones, where the bootstrapped (n=2000 iterations) 95% confidence interval for the slope of the best-fit line is [1.319, 1.486], encompassing larger values than what was obtained from the manually measured dataset.

Given the limited time and resources during the field campaign, comparatively larger stones were chosen for 3D scanning (cf. Fig. 2). Larger hailstones almost always have substantial wet growth layers (e.g., Knight and Knight 2005), during which more prominent icicle lobes may arise. Because the larger hailstones could be more irregularly shaped, could the 3D-scanner measurements be biased toward greater  $D_{\text{max}}$ ? To test this, we recomputed the bootstrapped 95% confidence interval about the slope of the best-fit line to the  $D_{\mathrm{max}}$  as a function of  $D_{\mathrm{eq}}$  data for the manually measured hailstones, but with all stones with  $D_{\rm eq} < 15\,{\rm mm}$  removed (i.e., removed any stone smaller than the smallest one in the 3D-scanned dataset). The removal of these smaller stones did not significantly change the mean slope, and only slightly widened the confidence interval to [1.141, 1.203]. Thus, the ellipsoidal geometry likely contributes more to the discrepancy between the manually measured and 3D-scanned datasets in best-fit line slopes. As such, we suggest that the "true" ratio between  $D_{\text{max}}$  and  $D_{\text{eq}}$  is somewhere between about

Additionally, for the 3D-scanned stones, as  $D_{\rm max}$  increases, the difference  $\delta D = D_{\rm max} - D_{\rm eq}$  tends to increase (r = [0.826, 0.918]; not shown). The slope of the best-fit line (0.33) implies

<sup>&</sup>lt;sup>1</sup> The Knight (1986) confidence intervals were computed with a *t* test, which strictly applies to a population characterized by a normal distribution.

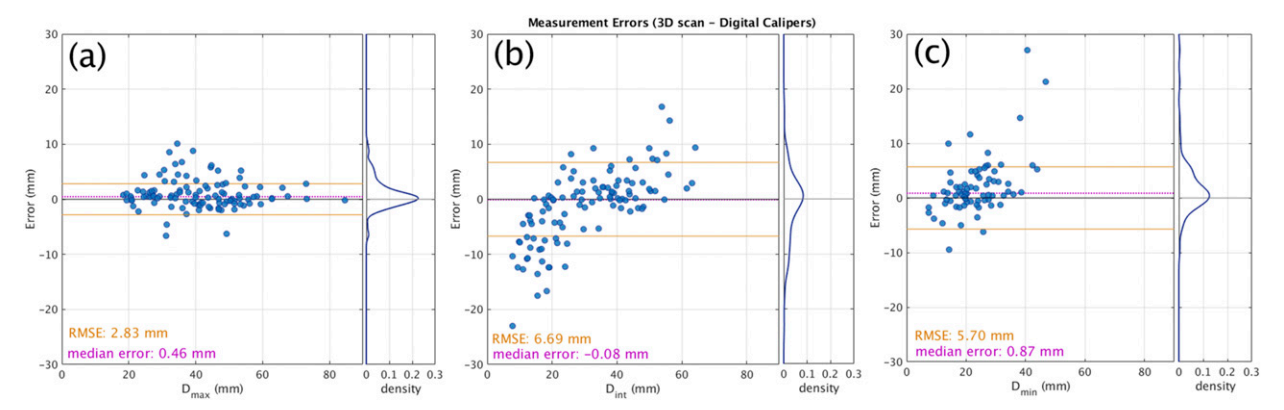


FIG. 4. Errors (defined as 3D-scanner measurement minus caliper measurement) for (a)  $D_{\rm max}$ , (b)  $D_{\rm int}$ , and (c)  $D_{\rm min}$ , shown as a function of the 3D-scanner measurement of that dimension. The magenta dotted line shows the median error, whereas the orange solid lines encompass plus and minus the RMSE value for each set. A kernel density estimate of the errors is shown to the right of each panel.

 $\delta D$  tends to be about a third of  $D_{\rm max}$ . Similarly, the manually measured hailstones feature a moderate correlation between  $\delta D$  and  $D_{\rm max}$  ( $r=[0.645,\,0.694]$ ; not shown), with a best-fit linear slope of 0.265. Large values of  $\delta D$  can imply greater irregularities or protuberances. This means that hailstones with

larger  $D_{\rm max}$  tend to be more irregular (i.e., nonspherical). Indeed, very large hailstones must have undergone significant periods of wet growth (e.g., Knight and Knight 2005; Kumjian et al. 2020), where prominent lobes or protuberances are thought to form.

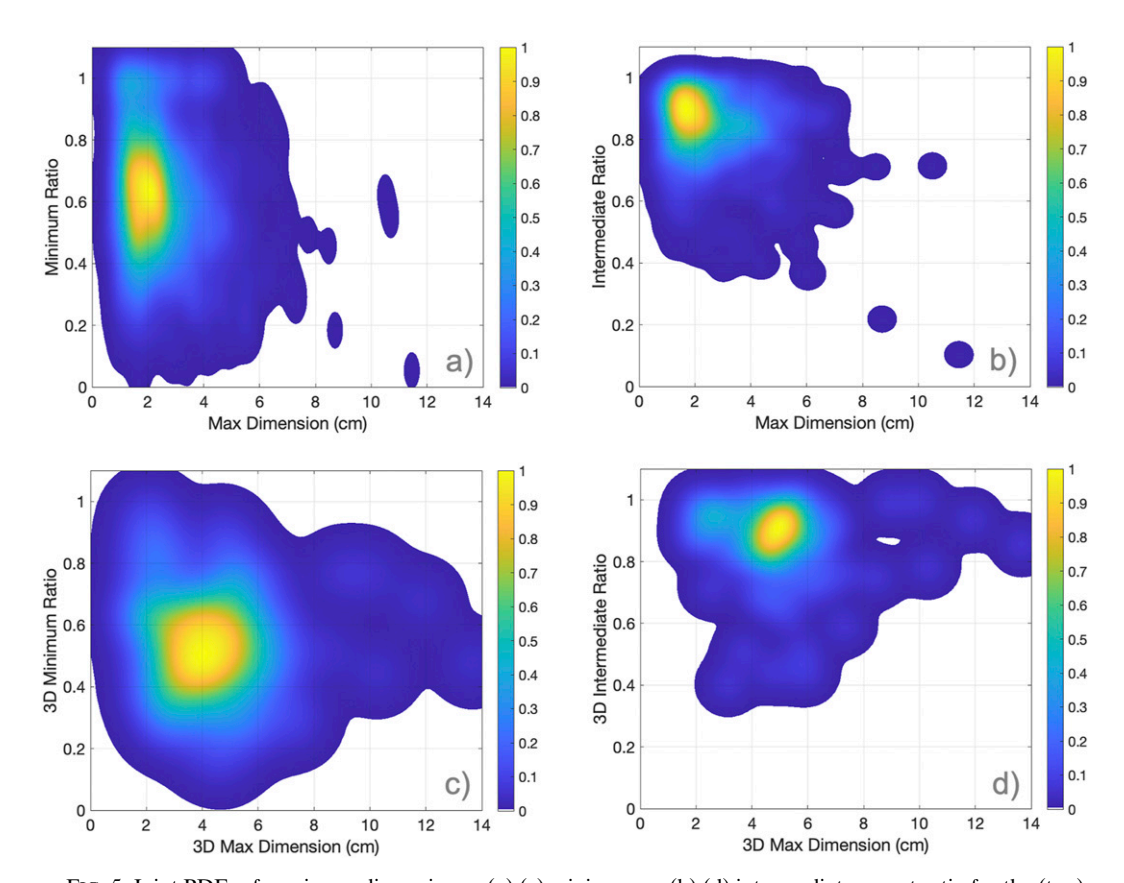


FIG. 5. Joint PDFs of maximum dimension vs (a),(c) minimum or (b),(d) intermediate aspect ratio for the (top) manually measured hailstones, where (a) n = 3689 (b) n = 1528, and (bottom) 3D-scanned hailstones, where (c),(d) n = 150. Distributions are shown as 2D kernel density estimates, with the densities normalized to the maximum value as indicated using the color bars to the right of each figure. The y axis has an upper limit of 1.1, which allows for some overshooting owing to how the kernel density is calculated.

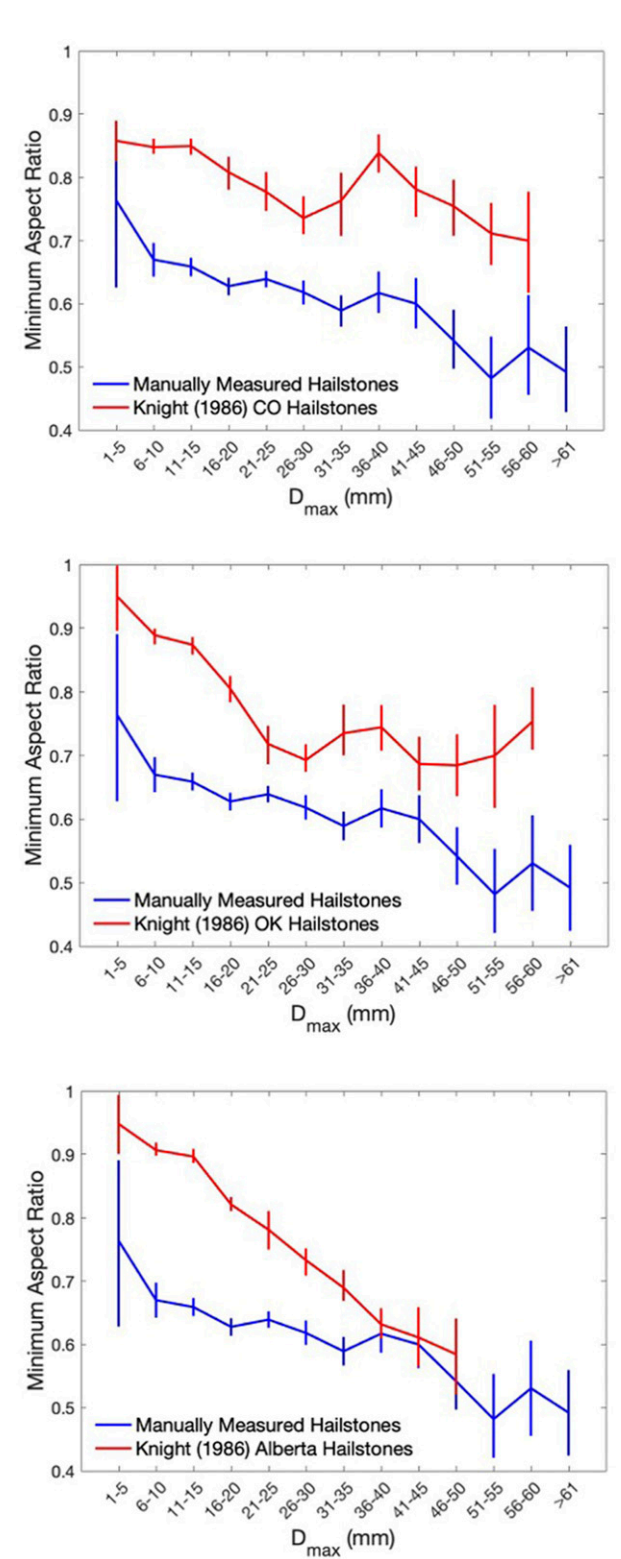
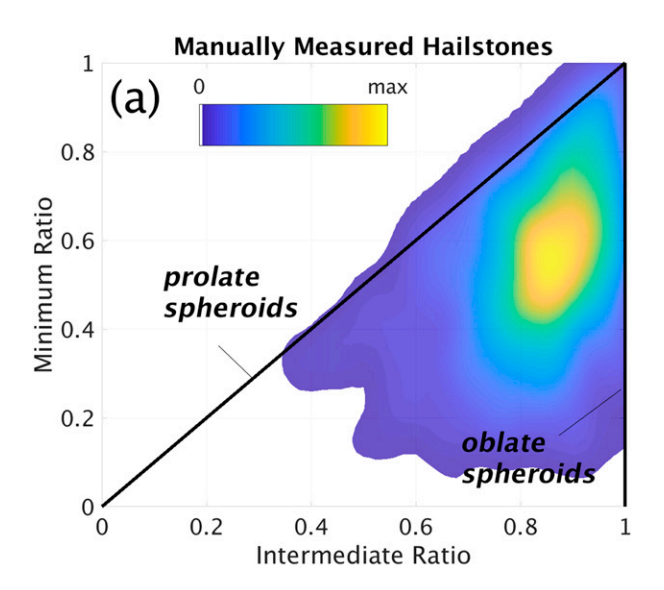


FIG. 6. Plots of  $D_{\rm max}$  vs minimum aspect ratio for the manually measured hailstones and the Knight (1986) hailstones from Colorado (n=1790), Oklahoma (n=2675), and Alberta (n=1743). Vertical bars represent the 95% confidence interval about the mean within each 5 mm size bin.



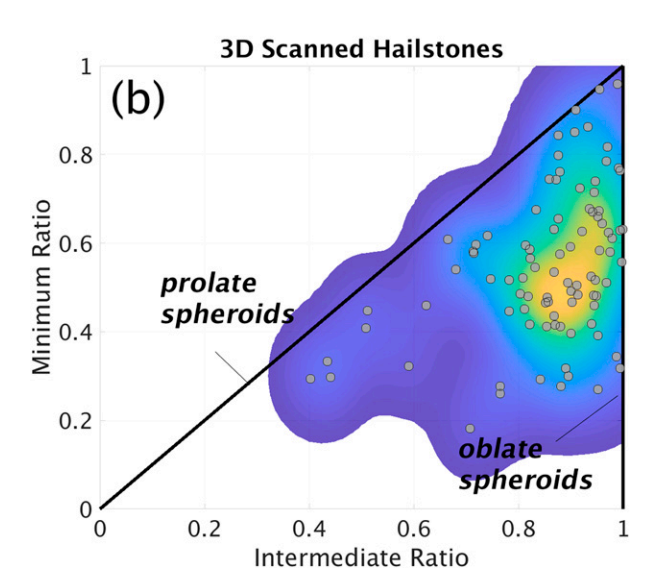


FIG. 7. Joint PDF of the intermediate vs minimum aspect ratios (shown as KDEs) for (a) the manually measured hailstones (n=1528) and (b) the scanned hailstones (n=150). The diagonal line represents prolate spheroids, the right vertical line represents oblate spheroids. Color shading shows density, with yellow values indicating the highest density, and dark blues the lowest. Individual data points shown in (b) as gray circle markers.

c. Ψ

The  $\Psi$  distributions as a function of  $D_{\rm max}$  are shown in Fig. 10 for both sets of hailstones. These are the first known reported  $\Psi$  values for natural hailstones.<sup>2</sup> For the manually measured

 $<sup>^2</sup>$  Note that, although reported as  $\Psi$ , the values shown in Fig. 5 of Heymsfield et al. (2018) are of measured volume divided by equivalent spherical volume, which is an alternative and not equivalent definition to the standard from Wadell (1935).

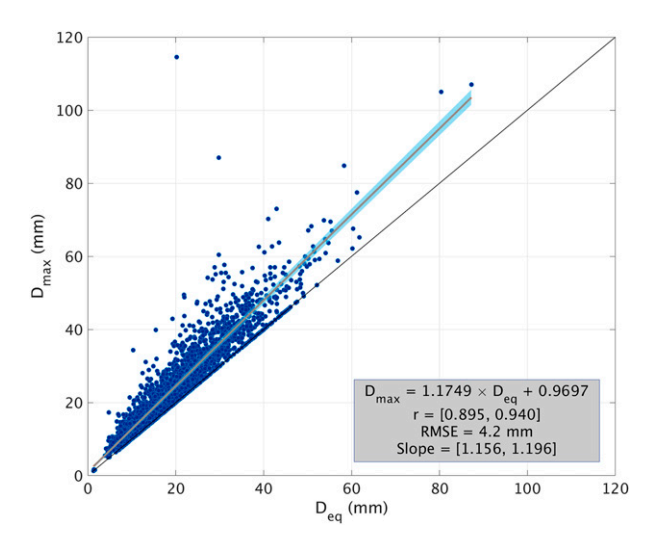


FIG. 8. Scatterplot of  $D_{\rm eq}$  vs  $D_{\rm max}$  for the manually measured hailstones (n=3689). The best-fit line is shown in orange, and the cyan shading represents the 95% confidence interval about the best-fit line. The inset box shows the equation for the best-fit line, the 95% confidence interval about the linear correlation coefficient r for the best-fit line, the RMSE, and the 95% confidence interval about the slope of the best-fit line.

hailstone dataset (Fig. 10a), a large majority of the hailstones have  $\Psi$  nearing 1, with a mean value of 0.9374. However, the distribution is broad, extending to much smaller values. Additionally, we see that  $\Psi$  decreases with increasing  $D_{\rm max}$ , which again suggests that larger hailstones are more likely to be less spherical in nature compared to their smaller counterparts.

For the 3D-scanned stones (Fig. 10b),  $\Psi$  varies from just below 1.0 to below 0.6, with the bulk of the distribution of points lying between 0.79 and 0.97. In other words, the bulk of the 3D-scanned hailstones exhibit 3%-27% greater surface areas than their equivalent-volume spherical counterparts, although some hailstones have >40%-50% enhancements. These 3D-scanned hailstones also reveal a decrease in  $\Psi$ , implying more irregular shapes or surfaces, with increasing  $D_{\text{max}}$ . The one outlier with the largest maximum dimension is the Vivian hailstone: the scan came from a plaster cast, which had a deteriorated shape relative to the actual stone (C. Knight 2014, personal communication). Thus, its  $\Psi$  value is likely an overestimate. With this outlier removed, the bootstrapped 95% confidence interval about the linear correlation is r =[-0.799, -0.631] and the best-fit line of  $\Psi$  as a function of  $D_{\rm max}$  has a decrease in  $\Psi$  of 0.023 mm<sup>-1</sup>.

# d. Drag coefficient and Reynolds number for 3D-scanned stones

The shapes of particles have an important role in their fall behavior, through the influence of shape on the drag coefficient,  $C_d$ . A hailstone's  $C_d$  is inversely proportional to its terminal velocity,  $v_t$ , so increasing the  $C_d$  will decrease the  $v_t$  and subsequently its kinetic energy. The lobes on a hailstone, which increase the roughness of the stone and can lead to more irregular shapes, have been shown to have an impact on its  $C_d$ .

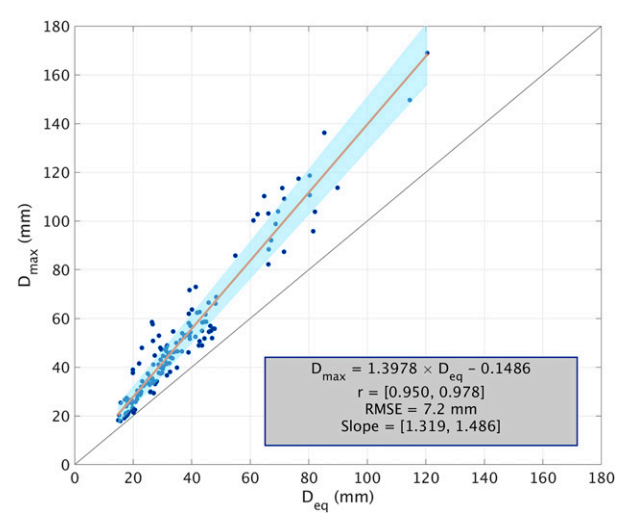


FIG. 9. As in Fig. 8, but for the 3D-scanned stones (n = 150).

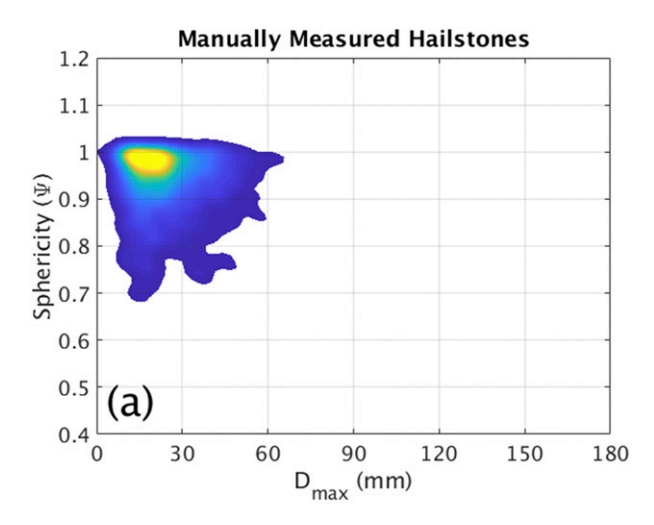
For example, a recent wind tunnel study using artificial, symmetrically lobed 3-cm maximum dimension particles (Theis et al. 2020) found that lobes of length 20% of the maximum dimension (i.e., 6 mm) resulted in  $C_d$  increases to  $\sim$ 0.57, larger than the value for the smooth 3-cm spheres of the same mass ( $\sim$ 0.45).

Often,  $C_d$  is parameterized as a function of the particle's Reynolds number

$$N_{\rm Re} = \frac{v_t D_p}{v}$$

where  $D_p$  is the particle's characteristic linear dimension, and  $\nu$  is the kinematic viscosity of the fluid within which the particle is embedded. Heymsfield et al. (2014) reviewed studies that found a "supercritical"  $N_{Re}$  exists, such that the  $C_d$  of the hailstone rapidly decreases at this value, and thus  $v_t$  rapidly increases; however, this only applied for smooth spheres. Roughening of spherical particles to emulate hailstones tends to damp out this  $C_d$  decrease. This suggests that natural hailstones, which, as we have shown above are not smooth spheres, do not have such a supercritical  $N_{Re}$ . Further, many of these studies (e.g., Heymsfield et al. 2014, 2018; Theis et al. 2020) employ a method using the Best number, which depends on the hailstone maximum dimension and cross-sectional area. The latter is challenging to estimate, given the uncertainties in hailstone fall behavior and detailed information on its shape. In contrast, the review study of Chhabra et al. (1999) found that the best predictor in  $N_{\mathrm{Re}}$ – $C_d$  relationships used the particle sphericity  $\Psi$ , which is also difficult to obtain in many cases. However, with the advent of 3D scans and the ability to accurately obtain  $\Psi$ , we can now explore how  $C_d$  might vary with  $N_{\rm Re}$  for natural hailstones. As such, for this analysis, only the 3D-scanned hailstones are used.

Determining the hailstone  $N_{\rm Re}$  is also challenging owing to the uncertainty associated with  $v_t$  (e.g., Heymsfield et al. 2018), as well as with  $D_p$  (i.e., which characteristic linear dimension to use?). For example, Heymsfield et al. (2018) recommend using



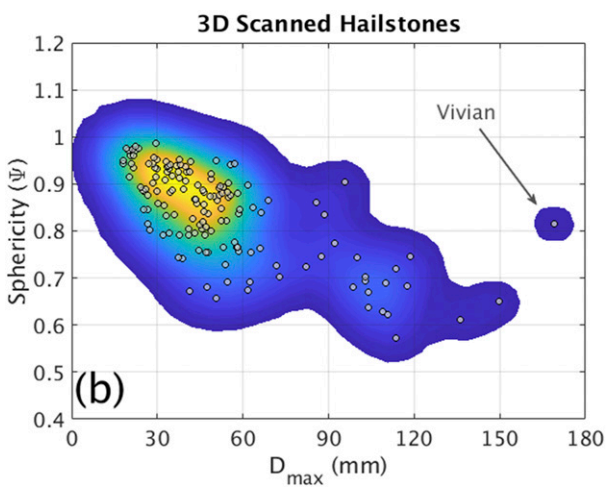


FIG. 10.  $D_{\rm max}$  vs  $\Psi$  for the (a) manually measured stones (n=3689) and (b) 3D-scanned stones (n=150). The individual data points are shown as gray circles.

 $D_{\rm max}$ , whereas Chhabra et al. (1999) argue  $D_{\rm eq}$  should be used. To account for this uncertainty, we will apply both in the analysis below. Additionally, we apply two hailstone fall speed–dimensional relationships: the latest from Heymsfield et al. (2018, corrigendum), and the one used in the Morrison 2-moment microphysics scheme (e.g., Morrison et al. 2009). In summary, we apply these two fall speed–dimensional relationships, and apply  $D_{\rm max}$  and  $D_{\rm eq}$  as the hailstone characteristic dimensions to both for a total of four combinations.

The distribution of  $C_d$  as a function of  $N_{\rm Re}$  is shown in Fig. 11. Overlaid for reference are the  $C_d$ - $N_{\rm Re}$  relationships for spheres from Ganser (1993) and Cheng (2009). There is no clear relationship between  $C_d$  and  $N_{\rm Re}$  in the 3D-scanned data (r < 0.25 for all combinations of  $D_p$  and  $v_t$ ). The distribution is centered on  $C_d$  values between 0.55 and 0.60, with the largest values exceeding 0.8. The  $C_d$  values calculated for natural hailstones with irregular shapes are distinctly greater than the expected values for spheres, indicating the influence of natural hailstone shape on  $C_d$ . These  $\Psi$ -based  $C_d$  values are in decent

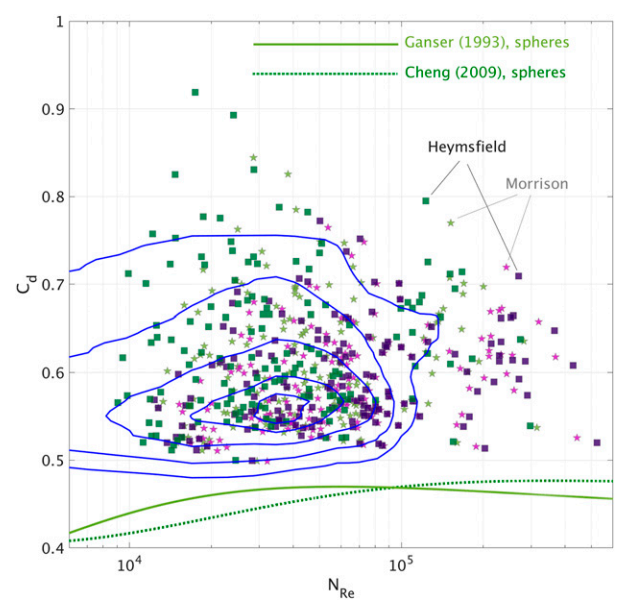


FIG. 11. Computed Reynolds number  $N_{\rm Re}$  vs drag coefficient  $C_d$ , based on measured sphericity values. The two green curves represent estimates for spheres from Ganser (1993) (solid) and Cheng (2009) (dashed). Two estimates for velocity are used: Morrison et al. (2005) (stars) and Heymsfield et al. (2018, corrigendum) (squares). The purple color indicates  $D_{\rm max}$  is used; green indicates  $D_{\rm eq}$  is used. Kernel density contours of 10%, 25%, 50%, 75%, and 90% of the data are overlaid in blue.

agreement with those found experimentally by Bailey and Macklin (1968b) (<0.66), Knight and Heymsfield (1983) (a bulk of their measurements were between 0.55 and 1.0), and Roos and Carte (1973) (range of 0.36 to 0.9), though somewhat higher than values reported in Heymsfield and Wright (2014) (0.4–0.45 for smaller hail) and lower than those reported in Matson and Huggins (1980) (0.65 to 1.3, with a mean of 0.87).

### 4. Discussion

The nonspherical nature of the hailstone shapes described above can give some insight into how such hailstones grow. Spheroidal hailstone shapes may indicate growth while rotating about the minor axis, which presumably is aligned in the horizontal (e.g., Macklin 1977). Asymmetries likely indicate hailstone fall behavior changes during its growth. Such a behavior is at odds with the conceptual model of radar-based studies, which often assume that hailstones are tumbling randomly (e.g., Bringi et al. 1984; Wakimoto and Bringi 1988; Kumjian and Ryzhkov 2008), or wobbling with their major axes oriented in the horizontal on average (e.g., Ryzhkov et al. 2011, 2013a,b). The nonspherical hailstone shapes indicate symmetric tumbling is not occurring.

Further, many studies in the radar community employing electromagnetic scattering calculations for polarization applications (e.g., Ryzhkov et al. 2011, 2013a,b; Kumjian et al. 2019) assume the hailstones to be spherical or spheroidal, in part owing to computational or software limitations. Assuming such

rotationally symmetric particles limits the diversity of shapes within the polarization plane, which results in the inability of these studies to accurately simulate observed polarimetric radar signatures. Instead, the use of triaxial ellipsoids in such studies would improve the ability to simulate radar signatures closer to what is observed. Of course, highly irregular or lobed particles further can affect the polarization characteristics of scattered radiation from hailstones and require more sophisticated treatments [see Jiang et al. (2019) for a discussion].

The simple linear relations between  $D_{\rm eq}$  and  $D_{\rm max}$ , as well as between  $\delta D$  and  $D_{\rm max}$  could be useful for parameterizing  $D_{\rm max}$  in hailstone growth models (e.g., Adams-Selin and Ziegler 2016; Dennis and Kumjian 2017; Kumjian and Lombardo 2020), which invariably predict spherical shapes and thus  $D_{\rm eq}$ . Such a mapping to  $D_{\rm max}$  affords more useful comparisons of hail growth models to hail report databases, which contain reports of hailstone  $D_{\rm max}$ .

The precisely measured  $\Psi$  values available from the 3Dscanned hailstone dataset reveal surface area enhancements, in some cases of over 50%, compared to equivalent-volume spheres, and that  $\Psi$  generally decreases with increasing  $D_{\text{max}}$ . This has important implications for growth and melting rates (e.g., Browning 1977). First, increased surface irregularities, as reflected in smaller  $\Psi$  values, imply a larger area of the surface capable of shedding turbulent wake, especially for the larger and thus faster-falling hailstones. Shedding of turbulence enhances the thermal energy transfer to or from the hailstone, and is typically quantified by the ventilation coefficient. Quantifying real hailstone  $\Psi$  values could help constrain idealized hailstone models used in wind tunnel studies, electromagnetic scattering calculations, or fluid dynamics computations, which often use rather unrealistic models (e.g., Mirković 2016; Wang and Chueh 2020; Theis et al. 2020). Second, the larger surface areas in general lead to enhanced thermal energy transfer rates because the heating/cooling rates are given by the thermal energy flux integrated over the surface area of the particle. These two factors lead to enhanced energy transfer rates and thus increased growth/melting rates compared to smoother or more spherical hail.

This study also showed the variability of  $C_d$  for a given  $N_{\rm Re}$ , ranging from 0.5 to 0.9. These values are larger than for spheres, which is unsurprising, given the rich nature of hailstone shapes and irregularities. This suggests that a one-size-fitsall approach (or one- $C_d$ -fits-all, as it were) may not adequately capture the true variability of natural hailstones. This is important, because Kumjian and Lombardo (2020) found a large sensitivity to  $C_d$  in their hailstone growth trajectory model, and  $C_d$  can strongly impact hailstone damage potential (e.g., Heymsfield et al. 2014). Further, variability in rimed ice fall speeds have enormous impacts on storm-scale numerical simulations (Morrison and Milbrandt 2011; Bryan and Morrison 2012). We suggest that including variability in  $C_d$ , especially for larger hailstones and/or those spent in significant periods of wet growth, is warranted for hail growth models, and for assessing hailstone damage potential (e.g., Heymsfield et al. 2014).

The dataset analyzed here provides insights into the natural variability of hailstone shapes. However, no dataset is without limitations. One such limitation of the dataset in our study comes from the potential of the hailstones melting in the field both before and during measurements. We can illustrate the potential impact melting may have on the data using the variability of hailstone properties across a hail swath during an example measurement IOP. Figure 12 shows such an example from a hail swath targeted during the IBHS field campaign from 5 June 2014 in eastern Colorado. The Storm Prediction Center issued a slight risk for severe thunderstorms that day, with a 15% chance for hail with  $D_{\text{max}} > 1$  in. (>2.5 cm). A severe thunderstorm warning was issued for this area at 2250 UTC (1650 MDT), warning for quarter-sized (1-in. or 2.5-cm) hail. The storm passed over the collection area between 2313 and 2346 UTC, with peak lowest-elevation angle radar reflectivity values >60 dBZ, suggestive of hail. Measurements by two IBHS teams were completed within 2.5 h of the storm passage, with the northern team moving south to north, and the southern team moving north to south. The largest hailstone of the 83 measured across this swath was 1.9 cm (or about 0.75 in.), which was at the southernmost location shown in Fig. 12. Because all 3 hailstone dimensions were measured during this IOP, both the intermediate and minimum aspect ratios were calculated. These aspect ratios, along with the  $D_{\text{max}}$ , were averaged over each of the 5 collection sites and plotted in Fig. 12 at their respective locations.

Overall, there is a decreasing trend in  $\varphi_{\min}$  as the teams progressed: the northern team's measurements reveal decreasing  $\varphi_{\min}$  of  $0.0048 \, \mathrm{min}^{-1}$  as they moved northward, and the southern team's measurements reveal decreasing  $\phi_{min}$ of  $-0.0052 \,\mathrm{min}^{-1}$  as they moved southward. These trends are coupled with a general decrease in both the average  $D_{\text{max}}$  and the overall  $D_{\max}$ , as one moves northward across the hail swath. This is despite the southernmost point being the latest measurement site for the southern team. That the maximum hail size is located on the southern periphery of the hail swath is consistent with expectations of fallout locations based on conceptual models of hail size sorting in right-moving supercell storms in the Northern Hemisphere (e.g., Browning and Foote 1976) and trajectory model calculations (e.g., Kumjian and Lombardo 2020). In contrast, the northward decrease in  $\varphi_{\min}$  in this case is more puzzling. We speculate that such a timedependent signal in the measurements seems to be plausibly an artifact of melting. Though we are unaware of detailed studies of hail melting while on the ground, it seems reasonable to speculate that surface melting could potentially impact the measured hailstone shapes. Specifically, we expect hailstones to "flatten out" or become more oblate as the part of the hailstone in contact with the warm ground<sup>3</sup> preferentially melts faster than the sides or top, which are exposed to the air. It is also expected that protuberances or lobes may melt faster than the hailstone body (e.g., Browning 1966), possibly increasing the sphericity and/or resulting in less exaggerated aspect ratios compared to freshly fallen hail. A conceptual model for such preferential melting is depicted schematically in Fig. 13.

 $<sup>^3</sup>$  This assumes hailstones have their  $D_{\text{max}}$  approximately level with the ground, which seems reasonable.

# 05 June 2014 Swath 1

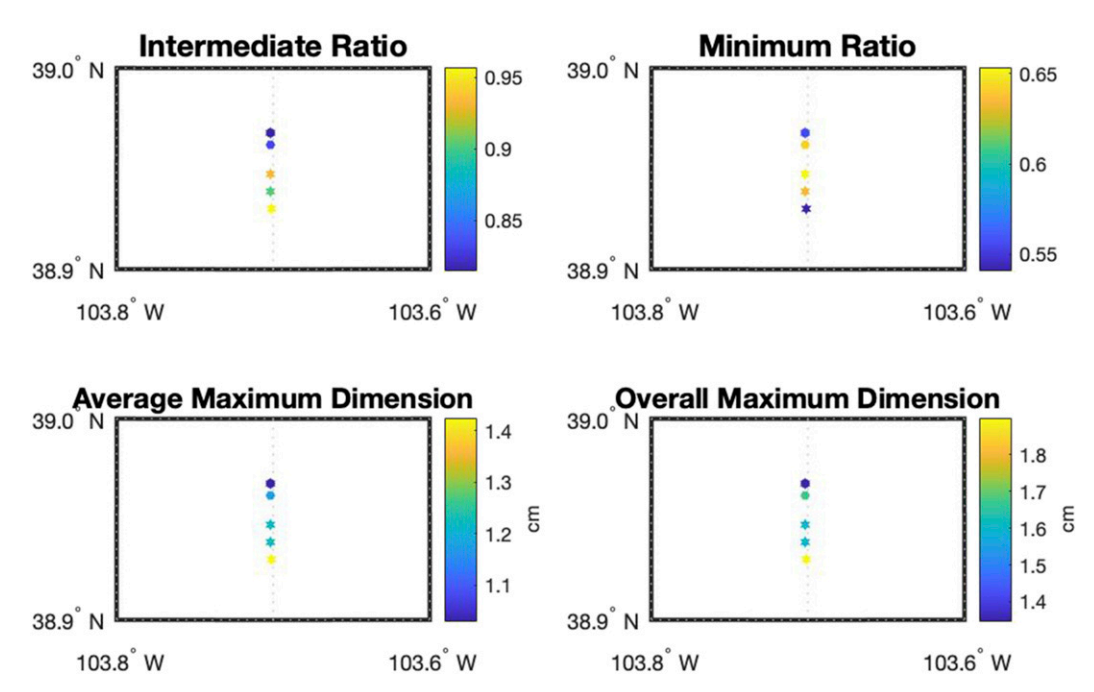


FIG. 12. Hailstone swath from 5 Jun 2014 in eastern Colorado showing (a) the average intermediate aspect ratio, (b) the average minimum ratio, (c) the average maximum dimension, and (d) the overall maximum dimension. n = 82. Two different teams were observing hailstones for this deployment: the top two points were one team and the bottom three were another team.

Additionally, rain may also lead to uneven melting of hailstones on the surface, affecting the hailstone shapes. The preferential melting and decreasing of the  $\varphi_{\min}$  with time could explain the discrepancy between our data and Knight (1986) seen in Fig. 6. Recall that the  $D_{\mathrm{int}}$  measurement errors were consistent with those of  $D_{\min}$ ; interestingly, for  $\varphi_{\mathrm{int}}$ , the southern collection team observed an increase with location, whereas the northern team observed a decrease similar to the other measured variables. This may be a reflection that  $\varphi_{\mathrm{int}}$  is less affected by melting while sitting on the surface.

This case is an illustrative example of trends sometimes observed in the field. Note that these trends were not consistent from swath to swath and in some cases, no clear hailstone shape and size trend was present. Nonetheless, we believe some data limitations are highlighted in this case.

### 5. Conclusions

Large datasets of manually measured hailstones (n=3689) and 3D laser-scanned hailstones (n=150) from the United States were analyzed to characterize and quantify the shapes of natural hailstones. The hailstones range in maximum dimension ( $D_{\rm max}$ ) from about <0.5 to >16 cm. Our analysis yields the following conclusions:

 Rather than spheres or spheroids, as is often assumed, triaxial ellipsoids or scalene oblate spheroids better represent hailstone shapes. These findings are consistent with previous studies with smaller sample sizes (e.g., Macklin 1977). In particular, the minor-to-major axis ratio tends to be between 0.4 and 0.8, with intermediate-to-major axis ratios between 0.8 and 1.0. The minor-to-major axis ratios are somewhat smaller than other datasets in the literature (Knight 1986), and may reflect prolonged melting on the surface prior to measurement.

- Hailstones become increasingly nonspherical with increasing size, as the aspect ratios and the sphericity of the hailstones decline with increasing  $D_{\rm max}$ .
- Strong, statistically significant positive correlations are found for the relationship between  $D_{\rm max}$  and spherical volume-equivalent diameter  $D_{\rm eq}$ , suggesting that  $D_{\rm max}$  is typically 20%–50% larger than  $D_{\rm eq}$ .
- For the first time, precise sphericity values are reported for real hailstones, obtained using 3D laser scanning technology. The sphericity values range from 0.57 to 0.99, with the peak in the distribution near 0.85. These sphericity values indicate enhancements in the hailstone surface area over that of the equivalent-volume sphere, which enhances vapor and thermal energy transfer to/from the hailstones, thus increasing the growth/melting rates over those assumed for spheres.
- These sphericity values are also used to obtain estimates of the drag coefficients of natural hailstones. The drag coefficients range from 0.5 to over 0.9; this range is substantially higher than the values for smooth spheres of similar Reynolds numbers (i.e., sizes), and has important implications for irregular hailstone fall speeds.

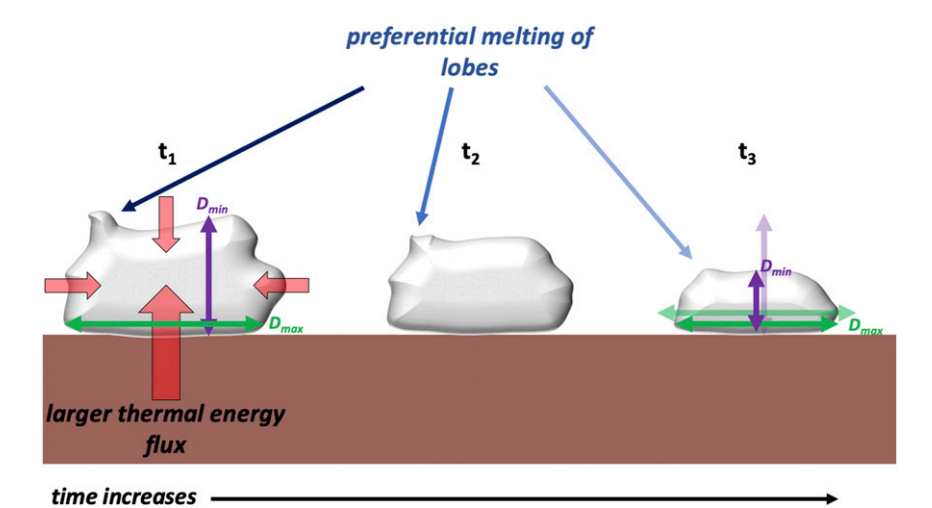


# FIG. 13. Schematic conceptual model for how hailstone melting on the ground (brown region) could lead to decreasing $\varphi_{\min}$ . Time increases from left to right. At the first time $(t_1)$ , the hailstone is freshly fallen and sits with its $D_{\max}$ (indicated by the green arrow) along the ground, and its $D_{\min}$ vertical (purple arrow). Owing to contact with the underlying surface, the bottom

natistone is freshly fallen and sits with its  $D_{\max}$  (indicated by the green arrow) along the ground, and its  $D_{\min}$  vertical (purple arrow). Owing to contact with the underlying surface, the bottom of the hailstone experiences a larger thermal energy flux (red arrows with sizes suggestive of magnitude). By time  $t_3$ , the  $D_{\min}$  has undergone a more substantial decrease than  $D_{\max}$ , leading to smaller  $\varphi_{\min}$ . Also of note is the diminished protuberance or lobe length, leading to larger  $\Psi$ .

Quantification of hailstone shapes is important because of their importance and relevance to microphysical processes, fall behaviors and fall speeds, and radar/satellite remote sensing. The data presented and analyzed here may help inform the parameterization or representation of hail in models and algorithms. We advocate for additional detailed measurements of hailstone shapes, especially with laser scanning. In particular, measurements of freshly fallen hail are needed to overcome the potential bias melting introduces in our dataset.

Acknowledgments. Support for the first and second authors of this research comes from a grant from the Insurance Institute for Business and Home Safety. The second author is also supported by NSF Grants AGS-1661679 and AGS-1855063. We thank the constructive comments from the three anonymous reviewers, which helped to clarify and strengthen this study. This work is part of the first author's research as an undergraduate student at The Pennsylvania State University.

### REFERENCES

Adams-Selin, R., and C. L. Ziegler, 2016: Forecasting hail using a one-dimensional hail growth model within WRF. Mon. Wea. Rev., 144, 4919–4939, https://doi.org/10.1175/MWR-D-16-0027.1.

Bailey, I. H., and W. C. Macklin, 1968a: Heat transfer from artificial hailstones. *Quart. J. Roy. Meteor. Soc.*, 94, 93–98, https:// doi.org/10.1002/qj.49709439910.

—, and —, 1968b: The surface configuration and internal structure of artificial hailstones. *Quart. J. Roy. Meteor. Soc.*, **94**, 1–11, https://doi.org/10.1002/qj.49709439902.

Barge, B. L., and G. A. Isaac, 1973: The shape of Alberta hailstones. *J. Rech. Atmos.*, **11**, 11–20.

Beyer, W. H., 2002: CRC Standard Mathematical Tables. 31st ed. CRC Press, 912 pp.

Bringi, V. N., T. A. Seliga, and K. Aydin, 1984: Hail detection with a differential reflectivity radar. *Science*, **225**, 1145–1147, https://doi.org/10.1126/science.225.4667.1145.

Brown-Giammanco, T., and I. Giammanco, 2018: An overview of the Insurance Institute for Business and Home Safety's hail research program. *29th Conf. on Severe Local Storms*, Stowe, VT, Amer. Meteor. Soc., 11.1, https://ams.confex.com/ams/29SLS/webprogram/Paper348661.html.

Browning, K. A., 1966: The lobe structure of giant hailstones. *Quart. J. Roy. Meteor. Soc.*, **92**, 1–14, https://doi.org/10.1002/qi.49709239102.

—, 1977: The structure and mechanisms of hailstorms. Hail: A Review of Hail Science and Hail Suppression, Meteor. Monogr., No. 38, 1–43.

——, and G. B. Foote, 1976: Air-flow and hail growth in supercell storms and some implications for hail suppression. *Quart. J. Roy. Meteor. Soc.*, **102**, 499–533, https://doi.org/10.1002/qi.49710243303.

Bryan, G. H., and H. Morrison, 2012: Sensitivity of a simulated squall line to horizontal resolution and parameterization of microphysics. *Mon. Wea. Rev.*, **140**, 202–225, https://doi.org/10.1175/MWR-D-11-00046.1.

Cheng, N.-S., 2009: Comparison of formulas for drag coefficient and settling velocity of spherical particles. *Powder Technol.*, 189, 395–398, https://doi.org/10.1016/j.powtec.2008.07.006.

Chhabra, R. P., L. Agarwal, and N. K. Sinha, 1999: Drag on nonspherical particles: An evaluation of available methods. *Powder Technol.*, **101**, 288–295, https://doi.org/10.1016/S0032-5910(98)00178-8.

Dennis, E. J., and M. R. Kumjian, 2017: The impact of vertical wind shear on hail growth in simulated supercells. *J. Atmos. Sci.*, **74**, 641–663, https://doi.org/10.1175/JAS-D-16-0066.1.

Efron, B., and R. J. Tibshirani, 1993: An Introduction to the Bootstrap. 1st ed. Chapman and Hall, 456 pp.

- Ganser, G. H., 1993: A rational approach to drag prediction of spherical and nonspherical particles. *Powder Technol.*, 77, 143–152, https://doi.org/10.1016/0032-5910(93)80051-B.
- Giammanco, I. M., T. M. Brown, R. G. Grant, D. L. Dewey, J. D. Hodel, and R. A. Stumpf, 2015: Evaluating the hardness characteristics of hail through compressive strength measurements. J. Atmos. Oceanic Technol., 32, 2100–2113, https://doi.org/10.1175/JTECH-D-15-0081.1.
- ——, B. R. Maiden, H. E. Estes, and T. M. Brown-Giammanco, 2017: Using 3D laser scanning technology to create digital models of hailstones. *Bull. Amer. Meteor. Soc.*, 98, 1341–1347, https://doi.org/10.1175/BAMS-D-15-00314.1.
- Heymsfield, A. J., and R. Wright, 2014: Graupel and hail terminal velocities: Does a "supercritical" Reynolds number apply? J. Atmos. Sci., 71, 3392–3403, https://doi.org/10.1175/JAS-D-14-0034.1.
- I. M. Giammanco, and R. Wright, 2014: Terminal velocities and kinetic energies of natural hailstones. *Geophys. Res. Lett.*, 41, 8666–8672, https://doi.org/10.1002/2014GL062324.
- ——, M. Szakáll, A. Jost I. Giammanco, and R. Wright, 2018: A comprehensive observational study of graupel and hail terminal velocity, mass flux, and kinetic energy. *J. Atmos. Sci.*, 75, 3861–3885, https://doi.org/10.1175/JAS-D-18-0035.1; Corrigendum. 77, 405–412, https://doi.org/10.1175/JAS-D-19-0185.1.
- Hong, S.-Y., and J. Lim, 2006: The WRF single-moment 6-class microphysics scheme (WSM6). J. Korean Meteor. Soc., 42, 129–151.
- Jiang, Z., M. R. Kumjian, R. S. Schrom, I. M. Giammanco, T. Brown-Giammanco, R. Maiden, and A. Heymsfield, 2019: Comparisons of electromagnetic scattering properties of real hailstones and spheroids. J. Appl. Meteor. Climatol., 58, 93– 112, https://doi.org/10.1175/JAMC-D-17-0344.1.
- Knight, C. A., and N. C. Knight, 1970: Lobe structures of hailstones. J. Atmos. Sci., 27, 667–671, https://doi.org/10.1175/ 1520-0469(1970)027<0667:LSOH>2.0.CO;2.
- —, and —, 2005: Very large hailstones from Aurora, Nebraska. Bull. Amer. Meteor. Soc., 86, 1773–1782, https://doi.org/10.1175/ BAMS-86-12-1773.
- Knight, N. C., 1986: Hailstone shape factor and its relation to radar interpretation of hail. J. Climate Appl. Meteor., 25, 1956–1958, https://doi.org/10.1175/1520-0450(1986)025<1956:HSFAIR> 2.0.CO;2.
- ——, and A. J. Heymsfield, 1983: Measurement and interpretation of hailstone density and terminal velocity. *J. Atmos. Sci.*, 40, 1510–1516, https://doi.org/10.1175/1520-0469(1983)040<1510: MAIOHD>2.0.CO;2.
- Kumjian, M. R., 2018: Weather radars. Remote Sensing of Clouds and Precipitation, C. Andronache, Ed., Springer-Verlag, 15-63.
- —, and A. V. Ryzhkov, 2008: Polarimetric signatures in supercell thunderstorms. J. Appl. Meteor. Climatol., 47, 1940–1961, https://doi.org/10.1175/2007JAMC1874.1.
- —, and K. Lombardo, 2020: A hail growth trajectory model for exploring the environmental controls on hail size: Model physics and idealized tests. *J. Atmos. Sci.*, 77, 2765–2791, https://doi.org/10.1175/JAS-D-20-0016.1.
- —, Z. J. Lebo, and A. A. Ward, 2019: Storms producing large accumulations of small hail. J. Appl. Meteor. Climatol., 58, 341–364, https://doi.org/10.1175/JAMC-D-18-0073.1.
- ——, and Coauthors, 2020: Gargantuan hail in Argentina. *Bull. Amer. Meteor. Soc.*, **101**, E1241–E1258, https://doi.org/10.1175/BAMS-D-19-0012.1.

- Macklin, W. C., 1963: Heat transfer from hailstones. *Quart. J. Roy. Meteor. Soc.*, **89**, 360–369, https://doi.org/10.1002/qj.49708938107.
- —, 1977: Characteristics of natural hailstones and their interpretation. *Hail: A Review of Hail Science and Hail Suppression, Meteor. Monogr.*, No. 38, 65–91, https://doi.org/10.1007/978-1-935704-30-0\_3.
- Matson, R. J., and A. W. Huggins, 1980: The direct measurement of the sizes, shapes, and kinematics of falling hailstones. *J. Atmos. Sci.*, **37**, 1107–1125, https://doi.org/10.1175/1520-0469(1980)037<1107:TDMOTS>2.0.CO;2.
- Mirković, D., 2016: Computational Electromagnetics for Polarimetric Radar Scatterers: An Approach to Polarimetric Variable Modeling of Hydrometeors and Biota. 1st ed. Lambert Academic Publishing, 272 pp.
- Morrison, H., and J. Milbrandt, 2011: Comparison of two-moment bulk microphysics schemes in idealized supercell thunderstorm simulations. *Mon. Wea. Rev.*, **139**, 1103–1130, https://doi.org/10.1175/2010MWR3433.1.
- —, and J. A. Milbrandt, 2015: Parameterization of microphysics based on the prediction of bulk ice particle properties. Part I: Scheme description and idealized tests. *Mon. Wea. Rev.*, 72, 287–311, https://doi.org/10.1175/JAS-D-14-0065.1.
- —, J. A. Curry, and V. I. Khvorostyanov, 2005: A new double-moment microphysics parameterization for application in cloud and climate models. Part I: Description. *J. Atmos. Sci.*, 62, 1665–1677, https://doi.org/10.1175/JAS3446.1.
- —, G. Thompson, and V. Tatarskii, 2009: Impact of cloud microphysics on the development of trailing stratiform precipitation in a simulated squall line: Comparison of one- and two-moment schemes. *Mon. Wea. Rev.*, 137, 991–1007, https:// doi.org/10.1175/2008MWR2556.1.
- Nelson, S. P., 1983: The influence of storm flow structure on hail growth. *J. Atmos. Sci.*, **40**, 1965–1983, https://doi.org/10.1175/1520-0469(1983)040<1965:TIOSFS>2.0.CO;2.
- Ortega, K. L., J. M. Krause, and A. V. Ryzhkov, 2016: Polarimetric radar characteristics of melting hail. Part III: Validation of the algorithm for hail size discrimination. *J. Appl. Meteor. Climatol.*, **55**, 829–848, https://doi.org/10.1175/JAMC-D-15-0203.1
- Rasmussen, R. M., and A. J. Heymsfield, 1987: Melting and shedding of graupel and hail. Part I: Model physics. *J. Atmos. Sci.*, **44**, 2754–2763, https://doi.org/10.1175/1520-0469(1987) 044<2754:MASOGA>2.0.CO;2.
- Roos, D. S., and A. E. Carte, 1973: The falling behavior of oblate and spiky hailstones. *J. Rech. Atmos.*, **7**, 39–52.
- Ryzhkov, A. V., M. Pinsky, A. Pokrovsky, and A. Khain, 2011: Polarimetric radar observation operator for a cloud model with spectral microphysics. *J. Appl. Meteor. Climatol.*, 50, 873– 894, https://doi.org/10.1175/2010JAMC2363.1.
- ——, M. R. Kumjian, S. M. Ganson, and A. P. Khain, 2013a: Polarimetric radar characteristics of melting hail. Part I: Theoretical simulations using spectral microphysical modeling. *J. Appl. Meteor. Climatol.*, **52**, 2849–2870, https://doi.org/10.1175/JAMC-D-13-073.1.
- —, —, and P. Zhang, 2013b: Polarimetric radar characteristics of melting hail. Part II: Practical implications. J. Appl. Meteor. Climatol., 52, 2871–2886, https://doi.org/10.1175/JAMC-D-13-074.1.
- Schuepp, P. H., and R. List, 1969: Mass transfer of rough hailstone models in flows of various turbulence models. *J. Appl. Meteor.*, 8, 254–263, https://doi.org/10.1175/1520-0450(1969)008<0254: MTORHM>2.0.CO;2.

- Theis, A., S. Borrmann, S. K. Mitra, A. J. Heymsfield, and M. Szakáll, 2020: A wind tunnel investigation into the aerodynamics of lobed hailstones. *Atmosphere*, 11 494, https:// doi.org/10.3390/atmos11050494.
- Thompson, G., R. M. Rasmussen, and K. Manning, 2004: Explicit forecasts of winter precipitation using an improved bulk microphysics scheme. Part I: Description and sensitivity analysis. *Mon. Wea. Rev.*, 132, 519–542, https://doi.org/10.1175/1520-0493(2004)132<0519:EFOWPU>2.0.CO;2.
- Wadell, H., 1935: Volume, shape and roundness of quartz particles. *J. Geol.*, **43**, 250–280, https://doi.org/10.1086/624298.
- Wakimoto, R. M., and V. N. Bringi, 1988: Dual-polarization observations of microbursts associated with intense convection: The 20 July storm during the MIST project. *Mon. Wea. Rev.*, **116**, 1521–1539, https://doi.org/10.1175/1520-0493(1988)116<1521: DPOOMA>2.0.CO;2.
- Wang, P. K., and C.-C. Chueh, 2020: A numerical study on the ventilation coefficients of falling lobed hailstones. *Atmos. Res.*, 234, 104737, https://doi.org/10.1016/j.atmosres.2019.104737.
- Ziegler, C. L., P. S. Ray, and N. C. Knight, 1983: Hail growth in an Oklahoma multicell storm. J. Atmos. Sci., 40, 1768–1791, https:// doi.org/10.1175/1520-0469(1983)040<1768:HGIAOM>2.0.CO;2.